ADVANCED FUNCTIONAL MATERIALS
www.afm-journal.de

Patterning Liquid Crystalline Organic Semiconductors via Inkjet Printing for High-Performance Transistor Arrays and Circuits

Xiaochen Fang, Jialin Shi, Xiujuan Zhang, Xiaobin Ren, Bei Lu, Wei Deng,* Jiansheng Jie, and Xiaohong Zhang**

Liquid crystalline (LC) organic semiconductors having long-range-ordered LC phases hold great application potential in organic field-effect transistors (OFETs). However, to meet real device application requirements, it is a prerequisite to precisely pattern the LC film at desired positions. Here, a facile method that combines the technique of inkjet printing and melt processing to fabricate patterned LC film for achieving high-performance organic integrated circuits is demonstrated. Inkjet printing controls the deposition locations of the LC materials, while the melt processing implements phase transition of the LC materials to form high-quality LC films with large grain sizes. This approach enables to achieve patterned growth of high-quality 2,7-dioctyl[1]-benzothieno[3,2-b][1]benzothiophene (C_8-BTBT) LC films. The patterned C_8-BTBT LC film-based 7 × 7 OFET array has 100% die yield and shows high average mobility of 6.31 $cm^2 V^{-1} s^{-1}$, along with maximum mobility up to 9.33 $cm^2 V^{-1} s^{-1}$. As a result, the inverters based on the patterned LC films reach a high gain up to 23.75 as well as an ultrahigh noise margin over 81.3%. Given the good generality of the patterning process and the high quality of the resulting films, the proposed method paves the way for high-performance organic integrated devices.

1. Introduction

Organic field-effect transistors (OFETs) as one of the prototypical organic electronic devices have found important applications in diverse fields, including displays, sensors, imagers, radio frequency identification (RFID), and logic circuits.[1–5] Among various organic semiconductors (OSCs) used in OFETs, liquid crystalline (LC) materials, such as benzothiophene (BTBT) derivatives, phenyl-terthiophene derivatives, and thiazole conjugated polymers, have attracted intensive interest due to their strong self-assembly ability to achieve long-range-ordered molecular packing.[6–13] This enables the formation of high-quality crystalline OSC thin films with larger aligned domains, fewer grain boundaries, and better in-plane π-π stacking.[14–17] More importantly, LC materials can rely on phase change from molten liquid to the crystalline state to attain the LC thin films.[11] Compared with solution-processed OSC films, the formation of LC thin films by phase transition would not experience the complex solvent evaporation process, avoiding the undesired "coffee-ring" effect.[12,18] Thus, the LC thin films can show better uniformity and more smooth surface morphology, which can effectively reduce the variation in the electrical performance of the devices.[13]

For the integrated device application, precisely patterning the LC thin films with desirable patterns and locations is a prerequisite. The use of patterned LC thin films can eliminate the parasitic currents and significantly decrease the transistor off current, thus leading to a larger noise margin of the constructed circuit.[19] Also, patterning of the LC thin films can facilitate the connection of the OFETs with other device elements for fabricating sophisticated circuits. However, it remains a challenge to rational pattern the LC thin films due to the difficulties in manipulating the molten liquid and controlling the subsequent film growth via phase transition. Among various patterning techniques, inkjet printing stands out because of its maskless patterning process, good resolution (≈50 µm), minimized material usage, and non-contact character.[20–26] To date, inkjet printing has been widely and actively used for patterning OSC thin film and inorganic semiconductor layers to demonstrate device applications.[27–31] Unlike inkjet-printed OSC films, inkjet printing of LC thin films requires the use of molten LC liquid as ink. Although the molten liquid can be conveniently obtained from heating the LC powders up to the melting point (above 100 °C), inkjet printing of patterned LC thin films would bring about a number of problems.[18,32] First, inkjet printing typically needs an ink with a viscosity value of about 10 cP.[33] However, the molten liquid is often of relatively high viscosity (100 cP), which

X. C. Fang, J. L. Shi, Prof. X. J. Zhang, X. B. Ren, B. Lu, Dr. W. Deng, Prof. J. S. Jie, Prof. X. H. Zhang
Institute of Functional Nano & Soft Materials (FUNSOM)
Jiangsu Key Laboratory for Carbon-Based Functional Materials & Devices
Soochow University
Suzhou, Jiangsu 215123, P. R. China
E-mail: xjzhang@suda.edu.cn; dengwei@suda.edu.cn; xiaohong_zhang@suda.edu.cn
Prof. J. S. Jie
Macao Institute of Materials Science and Engineering
Macau University of Science and Technology
Taipa, Macau SAR 999078, P. R. China
The ORCID identification number(s) for the author(s) of this article can be found under https://doi.org/10.1002/adfm.202100237.

DOI: 10.1002/adfm.202100237

severely degrades the jetting performance and thus will lose control of the deposited thin films.[34] Second, high temperature is always required to maintain the molten state of LC materials so that the inkjet printing cannot perform under ambient conditions. Moreover, directly heating the inkjet-printed nozzle is a great challenge. Therefore, the fabrication of LC thin film patterns by ejecting droplets of molten liquid (ink) from nozzles onto various substrates is impractical.

Here, we report, for the first time, a simple yet efficient printing technique to pattern LC thin films for high-performance OFET array and integrated circuits. This technique is based on a synergistic combination of inkjet printing and melt processing, referred to inkjet printing-assisted melt-processing (IJP-MP) method. In this method, inkjet printing of LC solution with the assistance of wetting/non-wetting patterned surfaces can precisely control their spatial localization. Then, melt processing is utilized to produce an isotropic liquid that can spontaneously spread out on the wetting surface. After cooling, recrystallization from the isotropic liquid phase occurs, yielding large single-crystalline domains with an average size of approximately 80 μm × 100 μm in the patterned thin films. The patterned LC films allow us to create an independently addressable OFET array with a yield of 100% and pseudo-complementary metal-oxide-semiconductor (CMOS) inverters. The 7 × 7 OFET array exhibits a high average mobility of 6.31 $cm^2\ V^{-1}\ s^{-1}$, along with a maximum mobility up to 9.33 $cm^2\ V^{-1}\ s^{-1}$. Due to the significant reduction of the cross-talk effects, the inverter based on the patterned LC films reaches a high gain up to 23.75 and an exceptionally large static noise margin (SNM) over 81.3%. Our work presents the great potential of the IJP-MP method for high-performance organic electronics.

2. Results and Discussion

C_8-BTBT composed of π-conjugated BTBT as a typical LC material was used in this study because of its high hole mobility and excellent stability.[35,36] **Figure 1**a–d shows the schematic illustration of the IJP-MP process for patterning C_8-BTBT LC films. First, C_8-BTBT solution ink (≈200 pL) was selectively printed onto the hydrophilic microtanks in the patterned photoresist (PR) template (see Experimental Section for details and Figure S1, Supporting Information). The deposited ink droplets would fill the microtanks on the patterned PR template and be confined in the hydrophilic areas (Figure 1a). The filled ink gradually evaporated, and eventually, a ring-like aggregation of crystals would form at the edge of the microtanks (Figure 1b) because of the well-known "coffee-ring" effect for the droplet during drying.[18,37] Then, the sample was heated above the melting temperature of the C_8-BTBT (102 °C) in air. At this temperature, the aggregated crystals were transformed into the isotropic liquid phase, which would spontaneously spread out to form thin liquid films within the microtanks (Figure 1c). After that, the sample was cooled down to 95 °C at a very slow cooling rate of 1 °C min^{-1}, enabling the phase transition of the isotropic liquid phase to crystal phase. The structural evolution from the isotropic liquid phase to C_8-BTBT crystal phase during the cooling process can be found in our previous work.[18] Finally, LC C_8-BTBT films were generated within each microtank, forming a patterned structure (Figure 1d).

The whole melting, spreading, and phase transition processes were revealed by using a polarized optical microscope (POM), as shown in Figure 1e and Movie S1, Supporting Information. The ring-like crystals at the edge of the microtanks are bright under POM observation. When the sample was heated close to the melting temperature (102 °C), part of the crystals was transformed into the isotropic liquid, along with the crystal luminescence vanished correspondingly. When the temperature reached 102 °C, the entire crystals had been melted, showing a complete extinction state in the POM image. Since the bottom of the microtanks has high surface energy, the molten C_8-BTBT liquid would continuously spread out toward the center of the microtanks. With the spreading of the C_8-BTBT liquid, a flat liquid film would form within the microtank. The above microscopic observations are consistent with the computational fluid dynamics (CFD) simulations (Figure 1f and Movie S2, Supporting Information). After that, the sample slowly cooled down to room temperature, and the C_8-BTBT molecules self-assembled into a uniform LC film with a thickness of about 45 nm within each microtank.

Figure 1g shows the POM image of the patterned 100 μm × 100 μm square C_8-BTBT LC films obtained from the IJP-MP method. All the C_8-BTBT LC films shine a bright light under the POM, indicating that every patterned C_8-BTBT LC film has a highly crystalline quality. Moreover, the C_8-BTBT LC films have uniformly covered the bottom of the microtanks. Most of the resulting C_8-BTBT LC films are composed of one large crystal domain along with several other small domains. Average size of the large crystal domains within each patterned C_8-BTBT LC film was 80 μm × 100 μm (Figure S2, Supporting Information). The relatively large crystal domains substantially reduce grain boundaries and stacking faults, which can promote efficient charge transport across the film. We also noted that in some patterns the C_8-BTBT LC film consisted of a single domain with its domain size as large as that of the microtank, as shown in Figure 1h,i. Atomic force microscope (AFM) image in Figure 1j exhibits that the crystal domain has a smooth surface morphology with many terrace structures. The lowest height of the terrace structure is ≈3.1 nm, corresponding to the molecular length along the long molecular axis of C_8-BTBT (Figure S3, Supporting Information). And the height of the highest terrace structure is about 9.8 nm, corresponding to 3 molecule lengths. This suggests that the C_8-BTBT molecules are aligned perpendicular to the substrate.

Crystallinity of the patterned C_8-BTBT LC films was examined through 2D-grazing incidence X-ray diffraction (2D-GIXRD) with a synchrotron X-ray source. The X-ray beam in the 2D-GIXRD has a size of ≈400 μm × 600 μm, thus allowing the detection of the entire structure of the C_8-BTBT LC film within each pattern. A schematic illustration of the 2D-GIXRD measurement is shown in **Figure 2**a. The sample was placed 265 mm away from the 2D CCD detector. The incident angle of an X-ray beam was set as 0.2° from the position of the reflected X-ray beam to the substrate. It was observed that the C_8-BTBT LC film produced high-order diffraction spots at the out-of-plane direction (q_z = 2.1, 4.3, and 6.5 nm^{-1}), which can be assigned as the (001), (002), and (003) planes, respectively (Figure 2b and

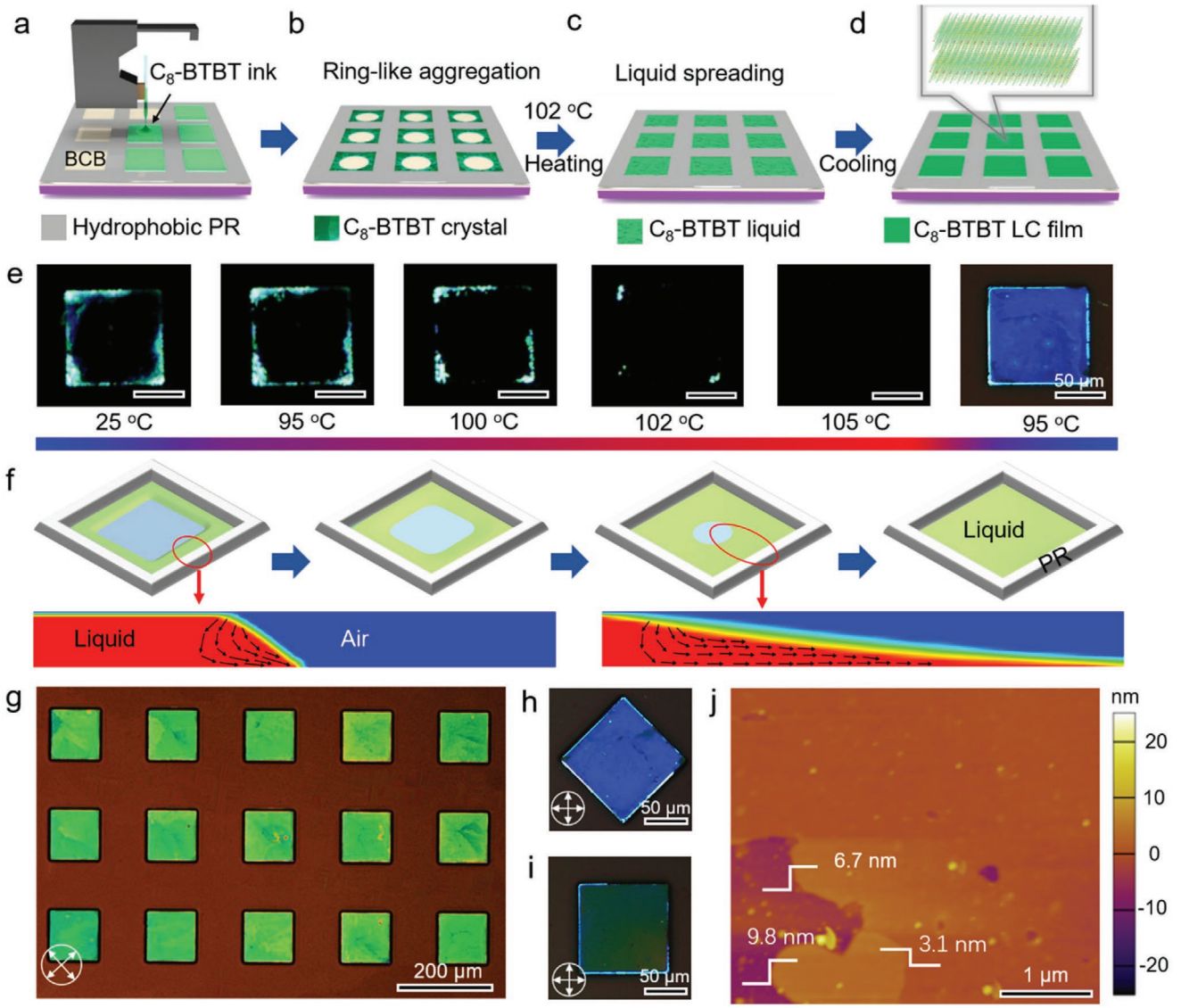

Figure 1. a–d) Schematic illustration of the patterning process of C_8-BTBT LC films using IJP-MP method. e) In situ POM observation of the melting process and recrystallization of the C_8-BTBT LC material in one microtank. The scale bar represents 50 μm. f) Simulation of the C_8-BTBT liquid spreading process. The arrow indicates the flow direction. g) POM image of a 3 × 5 array of C_8-BTBT LC films. h,i) POM images of the same C_8-BTBT LC film under 45° and 0° polarization angles, respectively. j) AFM image of the C_8-BTBT LC film.

Figure S4a, Supporting Information). The observation of only (00*l*) diffraction spots at the out-of-plane direction also suggests that the C_8-BTBT molecules have a stand-up orientation on the substrate. However, at the in-plane direction (q_{xy}), the patterned C_8-BTBT LC film generated a series of intense spot-like diffractions, which can be indexed to (01*l*), (100), (111), and (–112), respectively (Figure S4b, Supporting Information). The appearance of the spot-like diffraction indicates that the C_8-BTBT LC film at this detection area is single crystalline. In fact, we also observed the ring-like diffraction in other detection areas (Figure S5, Supporting Information). Therefore, it is confirmed that the C_8-BTBT LC film in each pattern is composed of one single-crystal domain or several domains with different orientations. Further, the structure of the crystal domains was examined by transmission electron microscopy (TEM) combined with selected-area electron diffraction (SAED). The low-resolution TEM image in Figure 2c reveals that the crystal domain has a large size with a smooth surface. SAED patterns obtained from four different positions in one crystal domain all present the same diffraction spots (Figure 2d,e), indicating its single-crystalline nature. In addition, high-resolution AFM (HR-AFM) images with an area of 10 × 10 nm^2 randomly collected from more than 50 positions at the C_8-BTBT LC film exhibit a very similar molecule packing mode (Figure 2f and Figure S6, Supporting Information). These results collectively demonstrate that the C_8-BTBT LC film is nearly in a single phase. Lattice constants could be calculated to be $a = 5.8 \pm 0.3$ Å, $b = 8.2 \pm 0.7$ Å, and $\gamma = 89.9° \pm 3.9°$ from the corresponding Fast Fourier Transform (FFT) patterns of the HR-AFM images (Figure 2g,h), which are consistent with reported C_8-BTBT LC crystal data.[29]

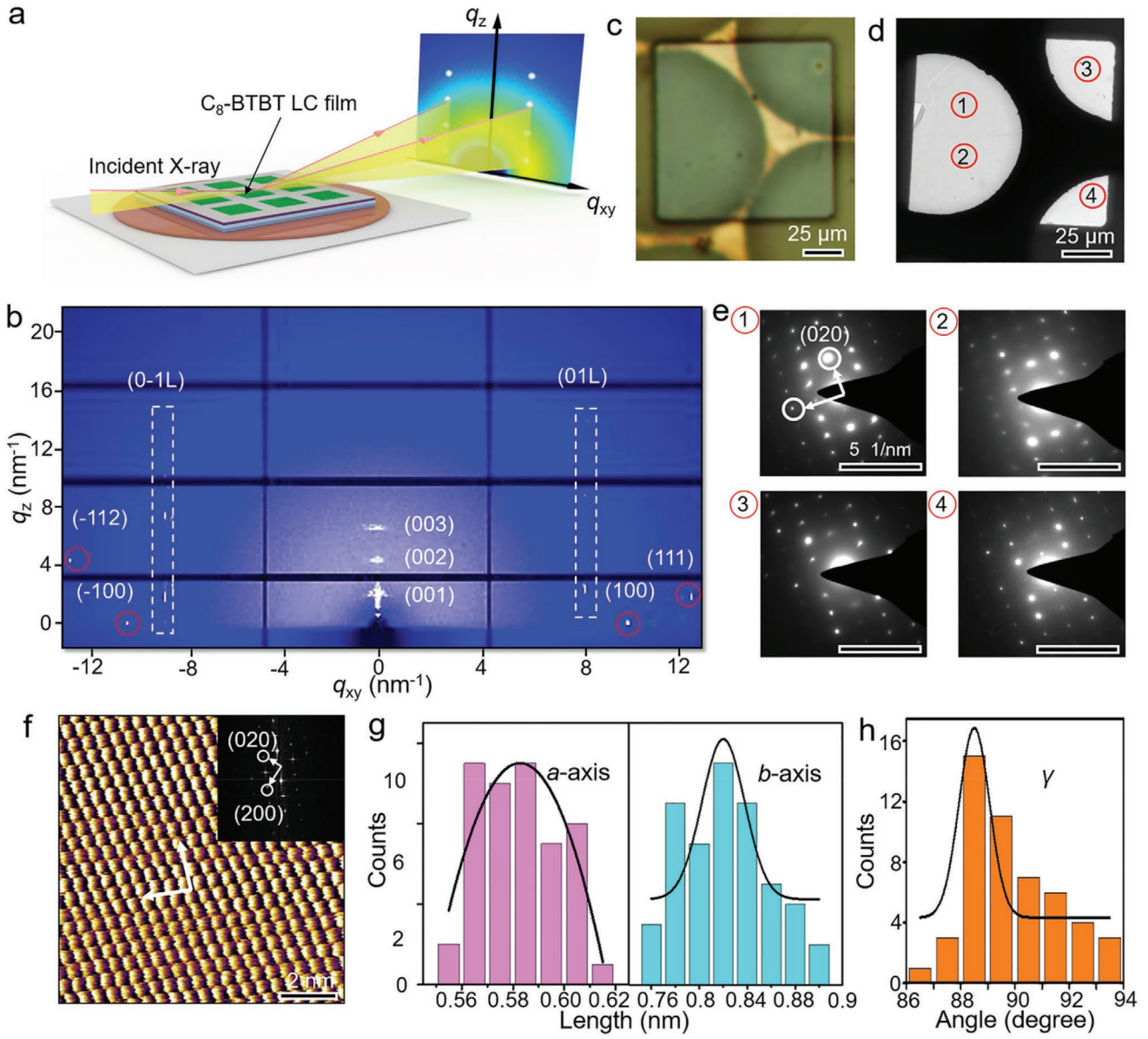

Figure 2. a) Schematic illustration of the GIXRD measurement configuration. b) 2D-GIXRD pattern of the patterned C_8-BTBT LC films. c,d) Optical microscopy and corresponding TEM image of the C_8-BTBT LC film on the Cu grid. e) SAED patterns collected from the marked areas (1–4) in (d). f) HR-AFM image of the C_8-BTBT LC film. g,h) Histogram of lattice constants of the obtained C_8-BTBT LC film.

Control of the wettability of the molten C_8-BTBT liquid on the microtank is critical for maintaining the shapes of the LC film with that of the pre-designed patterns. Therefore, we investigated four representative surfaces that have been widely used to deposit OSC thin films. The details and results of the calculated surface energies of different surfaces are shown in Figure S7 and Table S1, Supporting Information. For divinyltetramethyldisiloxane bis(benzocyclobutene) (BCB) and SiO_2 with high surface energies, the contact angles of the C_8-BTBT liquid are typically below 6° (**Figure 3**a), indicating the complete spreading of the C_8-BTBT liquid on the BCB and SiO_2 surfaces. As a result, a uniform C_8-BTBT LC film with 100% coverage could be obtained within each microtank, forming a pattern with the same shape as the pre-programmed template (Figure 3b). However, for the octadecyltrichlorosilane (OTS) and (tridecafluoro-1,1,2,2-tetrahydrooctyl)trichlorosilane (FTS) self-assembled monolayers (SAM), the C_8-BTBT liquid balls on the surfaces (Figure 3c), leading to some discontinuous C_8-BTBT crystals (Figure 3d).The wetting behavior of the C_8-BTBT liquid can be characterized quantitatively by the spreading coefficient (S)

$$S = \gamma_s - E_{ad} - E_{coh} \quad (1)$$

where γ_s is the surface energy of the substrate, E_{ad} represents the adhesive energy between the C_8-BTBT liquid and the substrate surface, E_{coh} refers to the cohesive energy of the C_8-BTBT liquid.[38] Figure 3e illustrates the different wetting behaviors of

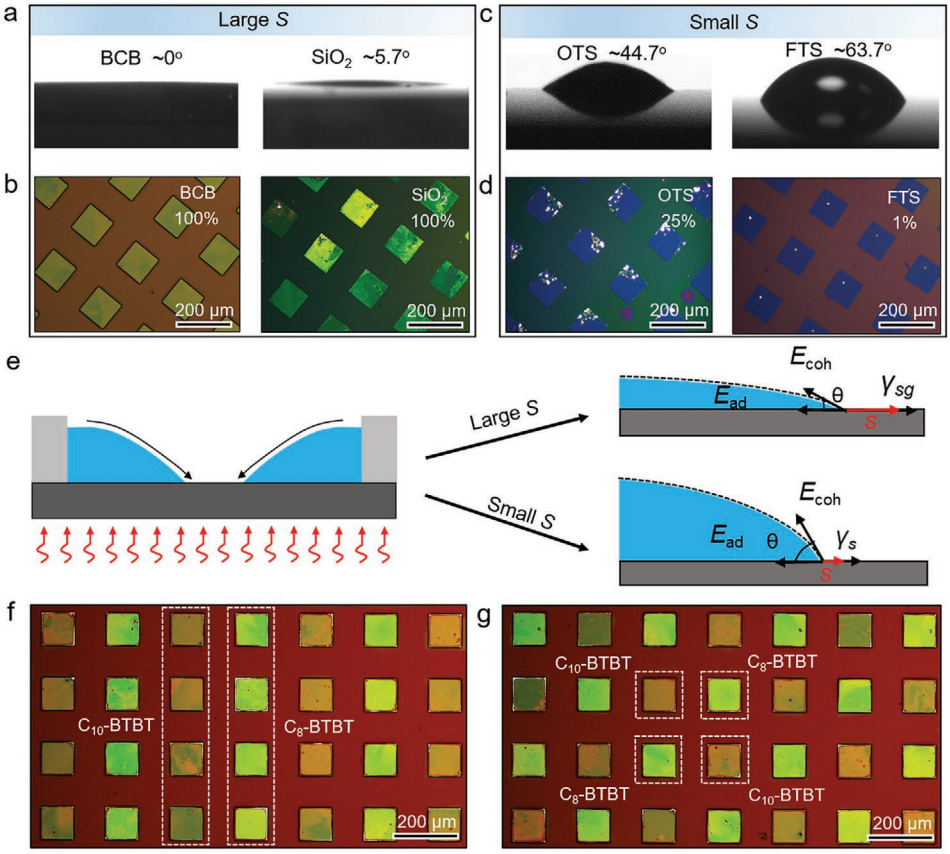

Figure 3. a,c) Contact angles of the molten C_8-BTBT liquid on the different surfaces. b,d) POM images of the obtained C_8-BTBT films using the different surfaces. e) Schematic illustration of the C_8-BTBT liquid wetting behaviors on the substrates with different surface energies. f,g) Optical microscope images of the patterned LC thin films consisting of C_{10}-BTBT and C_8-BTBT materials on the same substrate.

the C_8-BTBT liquid depending on S. If BCB or SiO_2 is used, the surface energy of the substrate (γ_s) is much higher than the sum of E_{ad} and E_{coh}, S is high enough for the molten C_8-BTBT liquid spread completely and form a uniform liquid film in the pattern. For OTS and FTS, their surface energies are relatively low and the corresponding S is small, which will lead to the partial spreading of the liquid. In this case, the C_8-BTBT liquid will shrink together within the microtanks. On the basis of the above results, it can be concluded that a high surface energy substrate is favorable for improving the spreading of the molten C_8-BTBT liquid for achieving high coverage of C_8-BTBT LC film on each pre-determined location, which also ensures the good pattern fidelity of the IJP-MP method. Because our proposed patterning method is based on inkjet printing, compared with other patterning methods,[19–26] it would allow us to integrate different kinds of LC materials on the same substrate. To demonstrate this, we performed the IJP-MP process using two kinds of LC materials, 2,7-didecylbenzothienobenzothiophene (C_{10}-BTBT) and C_8-BTBT. Different patterns consisting of both C_{10}-BTBT and C_8-BTBT LC films were successfully obtained on the same substrate (Figure 3f,g). This also confirms that the IJP-MP method could be applicable to other LC semiconductors.

The IJP-MP method is capable of depositing C_8-BTBT LC films with high-accuracy patterns.[20] This enables us to fabricate discrete OFETs with reduced crosstalk between adjacent devices.[39] **Figure 4**a shows the optical microscope image of the OFET array fabricated from the patterned C_8-BTBT LC films, where each pair of electrodes is bridged by a C_8-BTBT LC film. The OFETs adopted a bottom-gate top-contact configuration and were fabricated on the BCB (200 nm)-coved SiO_2/Si substrate. The total capacitance of the BCB/SiO_2 dielectric layer is measured to be 5.05 nF cm^{-2} (Figure S8, Supporting Information). Ag is used as the source (S) and drain (D) electrodes, and a layer of 2,3,5,6-tetrafluoro-7,7,8,8-tetracyanoquinodimethane (F_4-TCNQ) is inserted into the interface between the C_8-BTBT LC film and S/D electrodes to implement contact doping to reduce contact resistance. The channel length (L) and width (W) are 55 and 100 μm, respectively. The size of the crystal domain in the C_8-BTBT LC film is sufficiently large to cover the OFET channel (Figure 4b). As expected, it can substantially reduce grain boundaries and stacking faults and promote carrier transport. The transfer and output curves of one representative OFET in the 7 × 7 device array are shown in Figure 4c,d. The OFET displays an ideal p-type characteristic with excellent linearity, negligible hysteresis, and a low leakage current. The mobility extracted from the saturation regime reaches as high as 9.33 cm^2 V^{-1} s^{-1}, and I_{on}/I_{off} current ratio is estimated to be ≈10^5, along with a subthreshold swing of about 1.27 V dec^{-1}. The excellent electrical characteristics could be attributed to

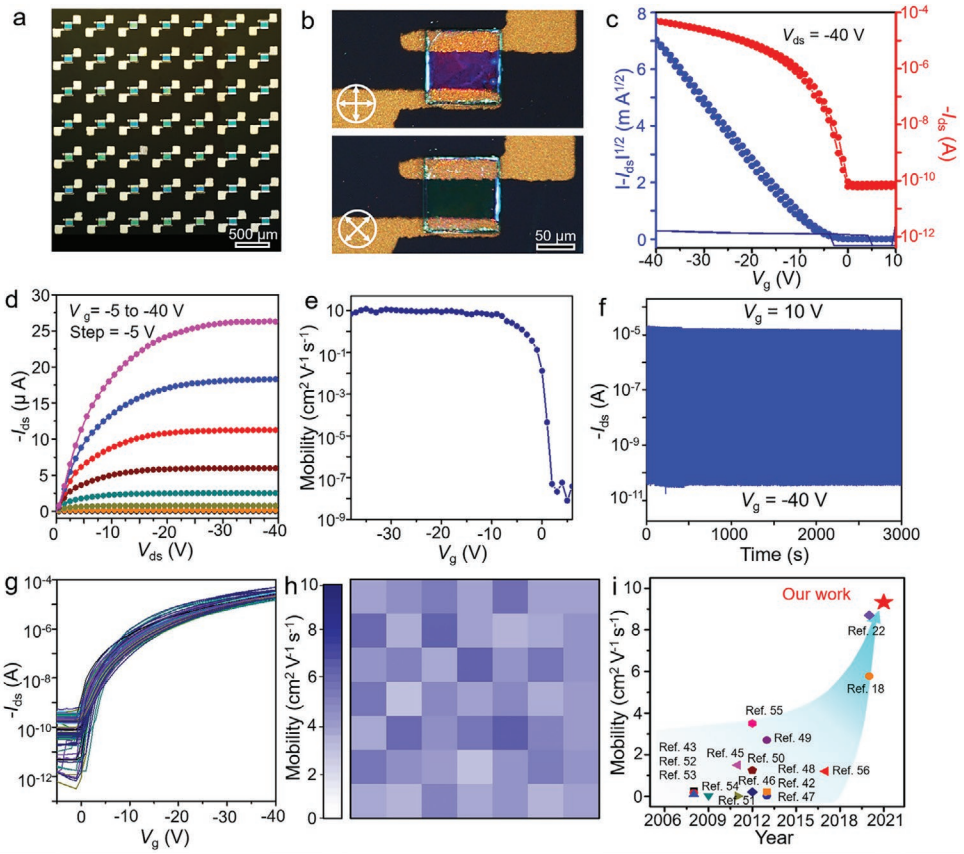

Figure 4. a) POM image of patterned C_8-BTBT LC film-based 7 × 7 OFET array. b) POM images of a typical OFET device. Representative c) transfer and d) output curves of an OFET from the 7 × 7 device array. e) Extracted mobility as a function of V_g. f) Operational cycle stability of a representative OFET in air. g) Transfer characteristics of the 49 OFETs recorded from the 7 × 7 device array. h) Spatial distribution of saturation mobilities of the 49 OFET devices. i) Comparison of the maximum mobilities of OFETs based on the patterned OSC films in the refs. [18,19,42–56] and in this work.

the high quality of the C_8-BTBT LC film. Figure 4e shows the saturation mobilities extracted at different gate voltages (V_g). It is seen that the mobility is almost gate-independent as V_g is above –6.4 V. Moreover, the device has a very small bias stress effect (Figure S9, Supporting Information), along with outstanding operating stability in the dark with a switching cycle of >3000 times at ambient conditions (Figure 4f). To further examine the yield of the working OFETs, we tested all the OFETs in the 7 × 7 device array. Figure 4g is a plot of overlaid transfer curves of the 49 OFETs measured at the saturation regions. Note that all the devices can work properly, reaching 100% yield with similar transfer curves, proving that the patterned OSC layers can effectively minimize the cross-talk between devices. The carrier mobility distribution in the 7 × 7 OFET array in Figure 4h shows quite a uniform color coverage, representing the high uniformity of the electrical performance of these devices. For the 7 × 7 device array, the average mobility is up to 6.31 cm^2 V^{-1} s^{-1} with a relative standard deviation of 21.5% (Figure S10, Supporting Information). Notably, the maximum mobility for the OFET array could be as high as 9.33 cm^2 V^{-1} s^{-1}, which is among the highest values reported for the discrete OFET array based on patterned OSC films, as shown in Figure 4i.

The uniform mobility distribution and high average mobility demonstrate the superiority of the patterned C_8-BTBT LC film-based OFETs for the integrated device application. As a proof of concept, we constructed a NOT gate circuit array, which was composed of 30 pseudo-CMOS inverters, as shown in **Figure 5**a,b. Each inverter integrated a pair of the OFETs in a common-source configuration, that is, a drive transistor (T_D), and a bias transistor (T_B), as illustrated in Figure 5c,d. Figure 5e shows a close-up optical microscope image of the fabricated inverter. POM images of both two C_8-BTBT LC films in the inverter exhibited simultaneous light extinction (Figure 5f), suggesting the device active layers consist of highly aligned crystalline films. Notably, the inverter shows a text-book voltage inversion characteristics at different supply voltage (V_{dd}) (Figure 5g). Voltage gain (dV_{out}/dV_{in}) is calculated from the voltage transfer curves, giving rise to a high gain of 23.75 at V_{DD} = 20 V (Figure 5h). The SNM is an important figure-of-merit for the circuit. Eliminating the cross-talk effect between adjacent devices would lead to a high SNM, ensuring the circuits function properly in specified noisy conditions.[19,40] The SNM is calculated by dividing the maximum length of a square fitted to the butterfly graph divided by $V_{DD}/2$, as displayed in Figure 5i. The inverter at V_{DD} = 15 V achieves a very large SNM of up to 81.3%, which represents the best result achieved for organic or metal oxide semiconductor-based inverters (comparison was made among previous works, see **Table 1**). The inverter array also shows a good uniformity in terms of gain; 90% of the 30 inverters exhibit gains over 15 (Figure S11,

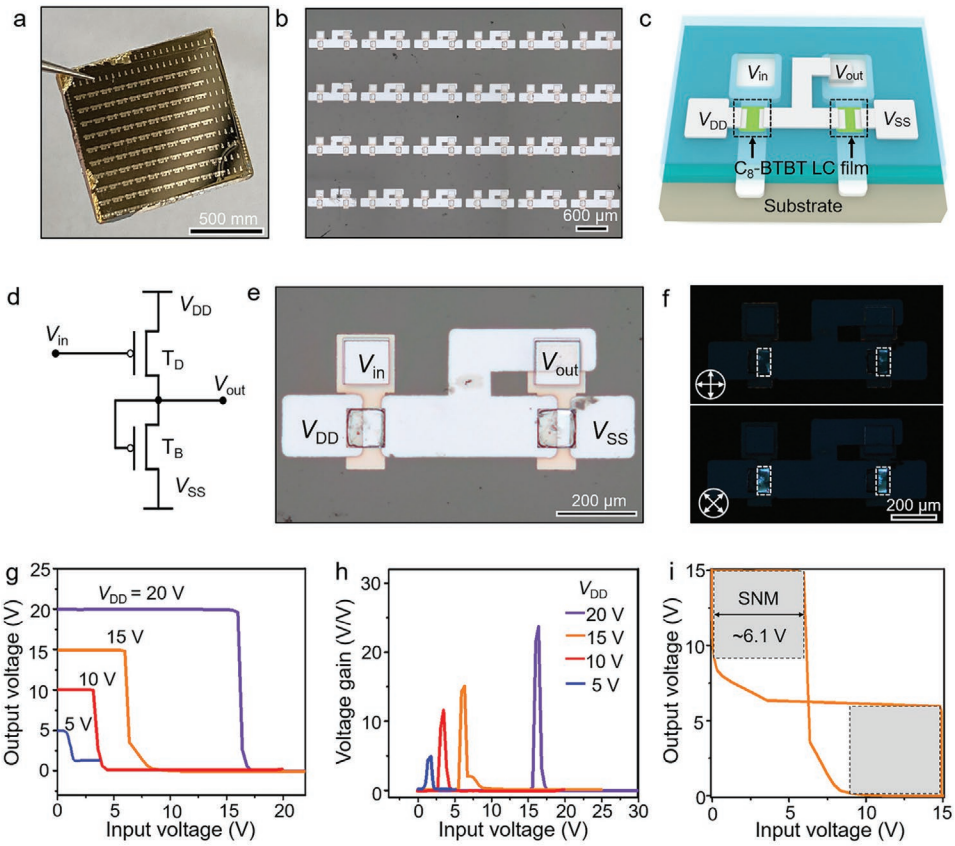

Figure 5. a) Photograph of the NOT gate circuit array based on patterned C_8-BTBT LC films. b) Optical microscope image of the NOT gate circuit array consisting of 30 pseudo-CMOS inverters. c) Schematic illustration of a pseudo-CMOS inverter made from the patterned C_8-BTBT LC films. d) Circuit diagram of a pseudo-CMOS inverter based on two p-type OFETs. e) Optical microscope image of the inverter. f) POM images of the pseudo-CMOS inverter circuit. g) Voltage input-output characteristics of the inverter and h) corresponding voltage gains at V_{DD} = 5, 10, 15, and 20 V, respectively. i) Butterfly inverter curves for SNM calculation at V_{DD} = 15 V.

Supporting Information). The good performance and high uniformity of the inverter array prove that the proposed patterning technique is applicable for the construction of more complicated logic circuits based on OSC films.

3. Conclusion

In summary, we have developed for the first time a flexible and facile IJP-MP method that combines inkjet printing and melt processing for patterning of LC thin films to achieve high-performance organic circuits. This method relies on inkjet printing with the assistance of hydrophilic microtanks to strictly control the deposition locations of the LC materials, followed by a melt processing to produce the phase transition of the LC materials for the fabrication of high-quality LC films with large grain size. As a result, precisely patterned C_8-BTBT thin films with large-sized single-crystalline domains were successfully achieved. The growth mechanism revealed that a high surface energy substrate could effectively improve the spreading area of the molten liquid and yield a uniform and 100% coverage C_8-BTBT thin film in each pattern. Based on the patterned C_8-BTBT LC films, high-performance OFET arrays with a yield of 100% were demonstrated. The 7×7 OFET array exhibited uniform electrical properties with a high average mobility of 6.31 $cm^2 V^{-1} s^{-1}$, along with a maximum mobility up to 9.33 $cm^2 V^{-1} s^{-1}$. Significantly, the patterned LC films effectively eliminated the cross-talk effect between adjacent devices, resulting in the inverter circuits with a high gain (>23.75) and an exceptionally high SNM over 81.3%. The SNM is among the highest values reported for the organic or metal oxide semiconductor-based inverters. The superiority of this approach to fabricate high-performance OFET arrays and circuits facilitates the applications of LC OSCs in organic electronic devices.

Table 1. Comparison of the SNM of inverters based on different materials and structures.

No.	Material	Structure	SNM	Ref.
1	C_8-BTBT	Pattern	81.3%	This work
2	Pentacene-ZnO	Film	76%	[57]
3	Tips-pentacene	Film	53.3%	[58]
4	Dif-TES-ADT	Pattern	75%	[59]
5	ZnO	Pattern	34%	[60]
6	C_8-BTBT	Pattern	80.1%	[19]

4. Experimental Section

Materials: C_8-BTBT and C_{10}-BTBT were purchased from Lumtec, China Taiwan, and were used as received. The C_8-BTBT solution was prepared by dissolving 5 mg C_8-BTBT in 1 mL chlorobenzene (HPLG, Sigma Aldrich). The C_{10}-BTBT solution was prepared by dissolving C_{10}-BTBT powder (5 mg mL^{-1}) in chlorobenzene. OTS and FTS were purchased from Sigma-Aldrich. BCB was purchased from Dow Chemicals.

Preparation of the Patterned PR Template: The patterned PR template with wetting microtanks was prepared as follows (Figures S1, Supporting Information). First, a positive PR (Allresist, AR-P5350) was spin-coated onto the BCB-covered SiO_2/Si substrate and annealed at 100 °C for 3 min. Subsequently, the substrate was transferred into a vacuum oven, and the PR layer was modified by using FTS vapor at 100 °C for 5 min, creating a superhydrophobic surface.

Then the substrate was exposed by UV light through a patterned mask with 100 μm × 100 μm squares. After that, the exposed parts of the PR layer were dissolved by a chemical developer (Allresist, AR300-26). Finally, patterned microtanks with a size of 100 μm × 100 μm were generated on the BCB-covered SiO_2/Si substrate.

Fabrication of the Pattern of C_8-BTBT LC Films: Controlled amounts of C_8-BTBT ink droplets were deposited on the microtanks in the patterned PR template using an inkjet printing system (Micro-nano material deposition inkjet printer system, Sonoplot's Microplotter Proto) equipped with an exact positioning program. Only the hydrophilic microtanks of the patterned PR template were filled with ink solutions. During drying of the ink, a ring-like aggregation of crystals formed at the edge of the PR. Then, the PR template along with the C_8-BTBT crystals was heated at 102 °C for 1 min. Last, the sample was cooled to 95 °C at a very slow cooling rate of 1 °C min^{-1}. This led to the formation of patterned LC C_8-BTBT films in the PR template.

Characterizations: Morphological characterization of the patterned LC C_8-BTBT films was performed by POM (Olympus, BX51), AFM (Asylum Research, Cypher S), and TEM (FEI, Tecnai G2-F20) at an accelerating voltage of 200 kV, and the preparation of the TEM sample was based on previous work.[41] The crystallinity of the LC C_8-BTBT films in the pattern was characterized by 2D-GIXRD. The 2D-GIXRD was performed at the Shanghai Synchrotron Radiation Facility (SSRF) on beamline BL14B1. The photon energy was 10 keV and the diffraction was recorded on a 2D CCD detector (Mar225 CCD). HR-AFM measurements were performed on an Asylum Cypher ES under ambient conditions using Asylum TR400PB tips.

Fabrication of OFET Array and Inverters: For the OFET array, a metal shadow mask was in alignment with the patterned LC C_8-BTBT films through a home-built mask alignment system. F_4-TCNQ (2 nm) and Ag (50 nm) were deposited by thermal evaporation under vacuum chamber pressure of 1×10^{-6} bar through the shadow mask. For the inverters, patterned Ag gate electrodes were fabricated by thermal evaporation and then patterned LC C_8-BTBT films were deposited on the gate electrodes. The metal shadow mask for the inverters was placed in alignment with the patterned LC C_8-BTBT films. Finally, the fabrication of the inverters was completed by thermal evaporation of 2 nm F_4-TCNQ and 50 nm Ag. The electrical characteristics of the devices were measured using a semiconductor parameter analyzer (4200SCS, Keithley) in ambient conditions.

Supporting Information

Supporting Information is available from the Wiley Online Library or from the author.

Acknowledgements

X.C.F. and J.L.S. contributed equally to this work. The authors thank the beamlines BL16B1 (Shanghai Synchrotron Radiation Facility) for providing the beamtime. This work was supported by the National Natural Science Foundation of China (Grant Nos. 51973147, 61904117, and 51821002), the Natural Science Foundation of Jiangsu Province of China (No. BK20180845), the Priority Academic Program Development of Jiangsu Higher Education Institutions (PAPD), and Collaborative Innovation Center of Suzhou Nano Science and Technology (Nano-CIC).

Conflict of Interest

The authors declare no conflict of interest.

Data Availability Statement

The data that supports the findings of this study are available in the supplementary material of this article.

Keywords

inkjet printing, inverters, liquid crystalline organic semiconductors, organic field-effect transistors, patterned growth

Received: January 9, 2021
Revised: February 19, 2021
Published online:

[1] S. Wang, J. Xu, W. Wang, G.-J. N. Wang, R. Rastak, F. M. Lopez, J. W. Chung, S. Niu, V. R. Feig, J. Lopez, T. Lei, S.-K. Kwon, Y. Kim, A. M. Foudeh, A. Ehrlich, A. Gasperini, Y. Yun, B. Murmann, J. B.-H. Tok, Z. N. Bao, *Nature* **2018**, *555*, 83.
[2] J. Kwon, Y. Takeda, R. Shiwaku, S. Tokito, K. Cho, S. Jung, *Nat. Commun.* **2019**, *10*, 54.
[3] J. W. Borchert, U. Zschieschang, F. Letzkus, M. Giorgio, R. T. Weitz, M. Caironi, J. N. Burghartz, S. Ludwigs, H. Klauk, *Sci. Adv.* **2020**, *6*, eaaz5156.
[4] S. Fratini, M. Nikolka, A. Salleo, G. Schweicher, H. Sirringhaus, *Nat. Mater.* **2020**, *19*, 491.
[5] C. Jiang, H. W. Choi, X. Cheng, H. B. Ma, D. Hasko, A. Nathan, *Science* **2019**, *363*, 719.
[6] H. Iino, J. Hanna, *Adv. Mater.* **2011**, *23*, 1748.
[7] E. B. Melo, J. Eccher, P. Apostol, H. Bock, I. H. Bechtold, *Mol. Cryst. Liq. Cryst.* **2017**, *657*, 81.
[8] K. Sun, Z. Y. Xiao, S. R. Lu, W. Zajaczkowski, W. Pisula, E. Hanssen, J. M. White, R. M. Williamson, J. Subbiah, J. Y. Ouyang, A. B. Holmes, W. W. H. Wong, D. J. Jones, *Nat. Commun.* **2015**, *6*, 6013.
[9] A. Kim, K. S. Jang, J. Kim, J. C. Won, M. H. Yi, H. Kim, D. K. Yoon, T. J. Shin, M. H. Lee, J. W. Ka, Y. H. Kim, *Adv. Mater.* **2013**, *25*, 6219.
[10] C. Zou, N. Yanahashi, Y. C. Wu, J. X. Wang, C. H. Zhang, G. R. Xiong, H. Yang, L. Jiang, T. Ikeda, *Adv. Funct. Mater.* **2018**, *28*, 1804838.
[11] H. Iino, J. Hanna, *J. Appl. Phys.* **2011**, *109*, 074505.
[12] R. Ozdemir, D. Choi, M. Ozdemir, H. Kim, S. T. Kostakoglu, M. Erkartal, H. Kim, C. Kim, H. Usta, *Chem. Phys. Chem.* **2017**, *18*, 850.
[13] H. Iino, T. Usui, J. Hanna, *Nat. Commun.* **2015**, *6*, 6828.
[14] M. Y. Lee, H. J. Kim, G. Y. Jung, A. R. Han, S. K. Kwak, B. J. Kim, J. H. Oh, *Adv. Mater.* **2014**, *27*, 1540.
[15] Y. Diao, B. C. K. Tee, G. Giril, J. Xu, D. H. Kim, H. A. Becerril, R. M. Stoltenberg, T. H. Lee, G. Xue, S. C. B. Mannsfeld, Z. N. Bao, *Nat. Mater.* **2013**, *12*, 665.
[16] M. J. Han, D. Y. Wei, Y. H. Kim, H. Ahn, T. J. Shin, N. A. Clark, D. M. Walba, D. K. Yoon, *ACS Cent. Sci.* **2018**, *4*, 1495.

[17] W. Deng, X. J. Zhang, H. L. Dong, J. S. Jie, X. Z. Xu, J. Liu, L. He, L. Xu, W. P. Hu, X. H. Zhang, *Mater. Today* **2019**, *24*, 17.
[18] W. Deng, Y. Lv, X. L. Zhang, X. C. Fang, B. Lu, Z. J. Lu, J. S. Jie, *Mater. Today* **2020**, *40*, 82.
[19] S. Duan, T. Wang, B. W. Geng, X. Gao, C. G. Li, J. Zhang, Y. Xi, X. T. Zhang, X. C. Ren, W. P. Hu, *Adv. Mater.* **2020**, *32*, 1908388.
[20] K. S. Park, J. Baek, Y. Park, L. Lee, Y. E. K. Lee, Y. Kang, M. M. Sung, *Adv. Mater.* **2016**, *28*, 2874.
[21] J. Kwon, Y. Takeda, R. Shiwaku, S. Tokito, K. Cho, S. Jung, *Nat. Commun.* **2019**, *10*, 54.
[22] A. Pierre, M. Sadeghi, M. M. Payne, A. Facchetti, J. E. Anthony, A. C. Arias, *Adv. Mater.* **2014**, *26*, 5722.
[23] J. T. Li, S. S. Delekta, P. P. Zhang, S. Yang, M. R. Lohe, X. D. Zhuang, X. L. Feng, M. Ostling, *ACS Nano* **2017**, *11*, 8249.
[24] M. Singh, H. M. Haverinen, P. Dhagat, G. E. Jabbour, *Adv. Mater.* **2010**, *22*, 673.
[25] J. K. Jiang, B. Bao, M. Z. Li, J. Z. Sun, C. Zhang, Y. Li, F. Y. Li, X. Yao, Y. L. Song, *Adv. Mater.* **2016**, *28*, 1420.
[26] S. R. Chen, M. Su, C. Zhang, M. Gao, B. Bao, Q. Yang, B. Su, Y. L. Song, *Adv. Mater.* **2015**, *27*, 3928.
[27] Z. K. Gu, K. Wang, H. Z. Li, M. Gao, L. H. Li, M. X. Kuang, Y. S. Zhao, M. Z. Li, Y. L. Song, *Small* **2017**, *13*, 1603217.
[28] P. W. Li, C. Liang, B. Bao, Y. N. Li, X. T. Hu, Y. Wang, Y. Q. Zhang, F. Y. Li, G. S. Shao, Y. L. Song, *Nano Energy* **2018**, *46*, 203.
[29] H. Minemawari, T. Yamada, H. Matsui, J. Tsutsumi, S. Haas, R. Chiba, R. Kumai, T. Hasegawa, *Nature* **2011**, *475*, 364.
[30] W. T. Xu, L. H. Wang, Y. W. Liu, S. Thomas, H. K. Seo, K. Kim, K. S. Kim, T. W. Lee, *Adv. Mater.* **2015**, *27*, 1619.
[31] J. T. Li, M. M. Naiini, S. Vaziri, M. C. Lemme, M. Östling, *Adv. Funct. Mater.* **2014**, *24*, 6524.
[32] J. C. Ribierre, Z. Li, X. Liu, E. Lacaze, B. Heinrich, S. Mery, P. Sleczkowski, Y. M. Xiao, F. Lafolet, D. Hashizume, T. Aoyama, M. Uchiyama, E. Zaborova, F. Fages, A. D. Aleo, F. Mathevet, C. Adachi, *J. Mater. Chem. C* **2019**, *7*, 3190.
[33] D. Kwak, H. H. Choi, B. Kang, D. H. Kim, W. H. Lee, K. Cho, *Adv. Funct. Mater.* **2016**, *26*, 3003.
[34] Y. H. Zhang, C. A. Fuentes, R. Koekoekx, C. Clasen, A. W. Vuure, J. D. Coninck, D. Seveno, *Langmuir* **2017**, *33*, 8447.
[35] Y. Wang, L. J. Sun, C. Wang, F. X. Yang, X. C. Ren, X. T. Zhang, H. L. Dong, W. P. Hu, *Chem. Soc. Rev.* **2019**, *48*, 1492.
[36] D. W. He, J. S. Qiao, L. L. Zhang, J. Y. Wang, T. Lan, J. Qian, Y. Li, Y. Shi, Y. Chai, W. Lan, L. K. Ono, Y. B. Qi, J. B. Xu, W. Ji, X. R. Wang, *Sci. Adv.* **2017**, *3*, e1701186.
[37] J. Q. Xiong, S. H. Li, J. H. Ciou, J. W. Chen, D. Gao, J. X. Wang, P. S. Lee, *Adv. Funct. Mater.* **2020**, *30*, 2006120.
[38] Q. Q. Wang, F. X. Yang, Y. Zhang, M. X. Chen, X. T. Zhang, S. B. Lei, R. J. Li, W. P. Hu, *J. Am. Chem. Soc.* **2018**, *140*, 5339.
[39] C. Wang, X. C. Ren, C. H. Xu, B. B. Fu, R. H. Wang, X. T. Zhang, R. J. Li, H. X. Li, H. L. Dong, Y. G. Zhen, S. B. Lei, L. Jiang, W. P. Hu, *Adv. Mater.* **2018**, *30*, 1706260.
[40] J. Kwon, Y. Takeda, K. Fukuda, K. Cho, S. Tokito, S. Jung, *ACS Nano* **2016**, *10*, 10324.
[41] W. Deng, X. J. Zhang, L. Wang, J. C. Wang, Q. X. Shang, X. H. Zhang, L. M. Huang, J. S. Jie, *Adv. Mater.* **2015**, *27*, 7305.
[42] D. Kwak, J. A. Lim, B. Kang, W. H. Lee, K. Cho, *Adv. Funct. Mater.* **2013**, *23*, 5224.
[43] J. A. Lim, W. H. Lee, H. S. Lee, J. H. Lee, Y. D. Park, K. Cho, *Adv. Funct. Mater.* **2008**, *18*, 229.
[44] M. Kano, T. Minari, K. Tsukagoshi, *Appl. Phys. Express* **2010**, *3*, 051601.
[45] X. R. Li, W. T. T. Smaal, C. Kjellander, B. Putten, K. Gualandris, E. C. P. Smits, J. Anthony, D. J. Broer, P. W. M. Blom, J. Genoe, G. Gelinck, *Org. Electron.* **2011**, *12*, 1319.
[46] M. Won Lee, G. S. Ryu, Y. U. Lee, C. Pearson, M. C. Petty, C. K. Song, *Microelectron. Eng.* **2012**, *95*, 1.
[47] T. Komino, H. Kuwabara, M. Ikeda, M. Yahiro, K. T. , C. Adachi, *Langmuir* **2013**, *29*, 9592.
[48] Y. Li, C. Liu, Y. Wang, Y. Yang, X. R. Wang, Y. Shi, K. Tsukagoshi, *AIP Adv.* **2013**, *3*, 052123.
[49] G. Giri, S. Park, M. Vosgueritchian, M. M. Shulaker, Z. N. Bao, *Adv. Mater.* **2014**, *26*, 487.
[50] Y. Li, C. Liu, A. Kumatani, P. Darmawan, T. Minari, K. Tsukagoshi, *Org. Electron.* **2012**, *13*, 264.
[51] Y. H. Kim, S. K. Park, *J. Inf. Disp.* **2011**, *12*, 199.
[52] T. Minari, M. Kano, T. Miyadera, S. D. Wang, Y. Aoyagi, M. Seto, T. Nemoto, S. Isoda, K. Tsukagoshi, *Appl. Phys. Lett.* **2008**, *92*, 173301.
[53] C. S. Kim, S. Lee, E. D. Gomez, J. E. Anthony, Y. L. Loo, *Appl. Phys. Lett.* **2008**, *93*, 103302.
[54] T. Minari, M. Kano, T. Miyadera, S. D. Wang, Y. Aoyagi, K. Tsukagoshi, *Appl. Phys. Lett.* **2009**, *94*, 093307.
[55] Y. Li, C. Liu, A. Kumatani, P. Darmawan, T. Minari, K. Tsukagoshi, *Mol. Cryst. Liq. Cryst.* **2012**, *556*, 13.
[56] F. Ge, X. H. Wang, Y. F. Zhang, E. Song, G. B. Zhang, H. B. Lu, K. Cho, L. Z. Qiu, *Adv. Electron. Mater.* **2017**, *3*, 1600402.
[57] B. Kumar, B. K. Kaushik, Y. S. Negi, *Microelectron. Reliab.* **2013**, *52*, 2801.
[58] J. Kwon, S. Kyung, S. Yoon, J. J. Kim, S. Jung, *Adv. Sci.* **2016**, *3*, 1500439.
[59] J. Kwon, Y. Takeda, K. Fukuda, K. Cho, S. Z. Tokito, S. Jung, *ACS Nano* **2016**, *10*, 10324.
[60] L. Lee, J. Hwang, J. W. Jung, J. Kim, H. I. Lee, S. Heo, M. Yoon, S. Choi, N. V. Long, J. Park, J. W. Jeong, J. Kim, K. R. Kim, D. H. Kim, S. Im, B. H. Lee, K. Cho, M. M. Sung, *Nat. Commun.* **2019**, *10*, 1998.